DOI: https://doi.org/10.14311/TPFM.2025.016

COMPARISON OF DIFFERENT LIMITERS IN MUSCL RECONSTRUCTION FOR THE NUMERICAL SOLUTION OF COMPRESSIBLE FLOW

Jiří Holman [1]

[1] **Department of Technical Mathematics, Faculty of Mechanical Engineering, Czech Technical University in Prague, Karlovo Náměstí 13, 12135 Prague, Czech Republic**

Abstract

The contribution deals with the comparison and selection of suitable limiter functions in MUSCL reconstruction, with a focus on high velocity compressible fluid flows. The numerical solution is obtained by the finite volume method based on the HLLC Riemann solver with the MUSCL reconstruction using different limiters. The limiter functions are first tested on the well-known transonic inviscid flow through the GAMM channel, then on the transonic turbulent flow past the RAE 2822 airfoil, and finally on the hypersonic viscous flow over a compressible ramp.

Keywords: transonic flow, hypersonic flow, HLLC, rotated-hybrid Riemann solver, finite volume method, MUSCL reconstruction, limiter.

1 Introduction

The finite volume method based on upwind discretization is a commonly used method for solving a wide range of computational fluid dynamics problems. Since schemes implementing upwind discretization are usually only first order accurate, they are usually used in combination with the reconstruction of unknown quantities. One of the most commonly used methods is the MUSCL[1] reconstruction [1]. Unfortunately, the reconstruction of unknown quantities introduces spurious oscillations into the solution near discontinuities or shocks, leading to instability and subsequent divergence of the numerical solution. Therefore, limiter functions are further used in the MUSCL reconstruction to prevent the generation and propagation of undesired oscillations.

The aim of this work is to test the performance and properties of various limiters, with particular emphasis on their use in the high-velocity flow of compressible fluids, i.e. especially for applications in high-velocity aerodynamics.

2 Governing equations

The flow of an inviscid compressible fluid is modeled by the system of Euler equations in vector form[2]

$$\frac{\partial W}{\partial t} + \frac{\partial F_j(W)}{\partial x_j} = 0, \qquad F_j(W) = \begin{pmatrix} \rho u_j \\ \rho u_i u_j + p\delta_{ij} \\ (\rho E + p)u_j \end{pmatrix}, \tag{1}$$

where $W = (\rho, \rho u_i, \rho E)^T$ is the vector of conservative variables, ρ is the density, u_i are components of the velocity vector, E is the total specific energy, p is the static pressure and δ_{ij} is the Kronecker delta.

The system of Euler equations (1) is closed by the equation of state of a perfect gas in the form

$$p = (\kappa - 1)\left[\rho E - \frac{1}{2}\rho u_j u_j\right], \tag{2}$$

where the gas constant[3] κ is assumed to be constant.

In the case of turbulent flows, the system of averaged Navier-Stokes equations is used. The

[1] Monotonic Upstream-centered Scheme for Conservation Laws.
[2] Summation over repeated indices will be used throughout the paper.
[3] In this work $\kappa = 1.4$.

vector form of these equations is as follows

$$\frac{\partial W}{\partial t}+\frac{\partial F_j(W)}{\partial x_j}=\frac{\partial R_j(W)}{\partial x_j},$$

$$F_j(W)=\begin{pmatrix}\rho u_j\\ \rho u_i u_j+p\delta_{ij}\\ (\rho E+p)u_j\end{pmatrix},\qquad R_j(W)=\begin{pmatrix}0\\ \tau_{ij}+\tau_{ij}^t\\ u_i(\tau_{ij}+\tau_{ij}^t)-(q_j+q_j^t)+d_j^t\end{pmatrix},$$

$$\tau_{ij}=\mu\left(\frac{\partial u_i}{\partial x_j}+\frac{\partial u_j}{\partial x_i}-\frac{2}{3}\delta_{ij}\frac{\partial u_k}{\partial x_k}\right),\qquad \mu=\mu_{ref}\left(\frac{p}{\rho}\right)^{\frac{3}{4}},\qquad \mu_{ref}=\text{const.},$$

$$q_j=-\frac{\kappa}{\kappa-1}\frac{\mu}{Pr}\frac{\partial}{\partial x_j}\left(\frac{p}{\rho}\right),\quad q_j^t=-\frac{\kappa}{\kappa-1}\frac{\mu_t}{Pr_t}\frac{\partial}{\partial x_j}\left(\frac{p}{\rho}\right),\quad d_j^t=(\mu+\sigma^*\mu_t)\frac{\partial k}{\partial x_j},\tag{3}$$

where $W=(\rho,\rho u_i,\rho E)^T$ is the vector of mean[4] conservative variables, $F_j(W)$ are the inviscid fluxes, $R_j(W)$ are the viscous fluxes, τ_{ij} are components of the viscous stress tensor, μ is the dynamic viscosity, q_j are components of the heat flux vector, q_j^t are components of the turbulent heat flux vector and d_j^t are components of the molecular diffusion and turbulent transport of the turbulent kinetic energy k [2]. Both the Prandtl number Pr and the turbulent Prandtl number Pr_t are assumed to be constant[5].

The model constant σ^*, the turbulent kinetic energy k, the turbulent viscosity μ_t and components of the Reynolds stress tensor τ_{ij}^t are modeled by the modified EARSM model of turbulence [3], [4], [5].

The system of averaged Navier-Stokes equations (3) is also closed with the equation of state of a perfect gas in the form

$$p=(\kappa-1)\left[\rho E-\frac{1}{2}\rho u_j u_j-\rho k\right].\tag{4}$$

3 Numerical method

The numerical solution is obtained by the in-house software based on the cell centered finite volume method [6] in semi-discrete form

$$\frac{dW_i}{dt}=\frac{1}{|D_i|}\sum_{k=1}^{\text{faces}}(\widehat{R}_k-\widehat{F}_k)\Delta S_k,\tag{5}$$

where W_i is an averaged solution over the cell D_i, viscous flux $\widehat{R}=\vec{R}\cdot\vec{n}$, inviscid flux $\widehat{F}=\vec{F}\cdot\vec{n}$, ΔS is the area of the cell face between two adjacent cells and $\vec{n}$ is the unit vector normal to a face.

The inviscid flux is approximated by the modified[6] HLLC Riemann solver [7], [2]. High order accuracy in space is achieved by the MUSCL reconstruction ([1], [8]) of the primitive variables $U=(\rho,u_i,p)^T$ in form

$$\widetilde{U}_L = U_L+\frac{1}{4}\left[(1-\vartheta)\phi(r_L)\overleftarrow{\Delta}_L+(1+\vartheta)\phi\left(\frac{1}{r_L}\right)\overrightarrow{\Delta}_L\right],\tag{6}$$

$$\widetilde{U}_R = U_R-\frac{1}{4}\left[(1-\vartheta)\phi(r_R)\overleftarrow{\Delta}_R+(1+\vartheta)\phi\left(\frac{1}{r_R}\right)\overrightarrow{\Delta}_R\right],\tag{7}$$

where $\overrightarrow{\Delta}_L=U_R-U_L$ and $\overleftarrow{\Delta}_L=U_L-U_D$, see figure 1, and $r=\overrightarrow{\Delta}/\overleftarrow{\Delta}$. The MUSCL reconstruction is applied as a one-dimensional reconstruction in each direction.

By selecting the parameter ϑ, it is possible to obtain different schemes [1]. In this work the value $\vartheta=1/3$ is chosen, as this theoretically leads to the third order accurate upwind scheme. The third order accuracy could be obtained on a regular computational grid with a sufficiently smooth

[4]Reynolds averaging is used for density and static pressure and Favre averaging is used for total specific energy and for components of the velocity vector [4].

[5]In this work $Pr=0.72$ and $Pr_t=0.9$.

[6]More specifically, the HLLC scheme with low Mach number fix.

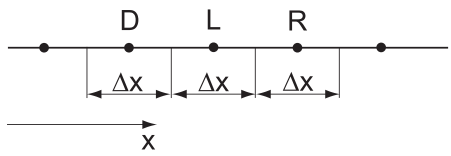

Figure 1: Computational stencil of MUSCL reconstruction in x-axis direction.

solution, which is not the case for the problems solved in this work. However, even in the case of irregular grids and shock-dominated solutions, the MUSCL reconstruction (with $\vartheta = 1/3$) usually provides a more accurate approximation than the other options.

The HLLC scheme with MUSCL reconstruction can be numerically unstable as it tends to oscillate strongly close to the shocks or discontinuities. Therefore, a so-called limiter function $\phi(r)$ is introduced, which switches back to the first-order scheme in the vicinity of shocks or steep gradients in the solution. The following limiter functions are investigated in this paper:

- Koren limiter (third-order accurate for sufficiently smooth solution [9])

$$\phi(r) = \max\left[0, \min\left(2r, \frac{1+2r}{3}, 2\right)\right]. \tag{8}$$

- MC (monotonized central) limiter

$$\phi(r) = \max\left[0, \min\left(2r, \frac{1+r}{2}, 2\right)\right]. \tag{9}$$

- Minmod limiter

$$\phi(r) = \max[0, \min(1, r)]. \tag{10}$$

- Osher limiter (the constant C_β can be chosen from the interval $(1, 2)$)

$$\phi(r) = \max[0, \min(C_\beta, r)], \tag{11}$$

- Ospre limiter

$$\phi(r) = \frac{1.5(r^2 + r)}{r^2 + r + 1}. \tag{12}$$

- Superbee limiter

$$\phi(r) = \max\left[0, \min(2r, 1), \min(r, 2)\right]. \tag{13}$$

- van Albada limiter

$$\phi(r) = \frac{r + r^2}{1 + r^2}. \tag{14}$$

- van Leer limiter

$$\phi(r) = \frac{r + |r|}{1 + |r|}. \tag{15}$$

The viscous flux is discretized by the central scheme with the aid of diamond shape dual cells [10]. The time integration of the semi-discrete finite volume method (5) is done by the explicit two-stage strong stability preserving (SSP) Runge-Kutta method [11].

4 Transonic inviscid flow through the GAMM channel

The first case solved is the well-known transonic flow of the inviscid compressible fluid through the GAMM channel, which is often used as a validation test case. The flow is characterized by a ratio of outlet pressure and stagnation pressure $p_2/p_0 = 0.737$ and a zero angle of attack. A structured H-type grid is used, with refinement in the second half of the channel, consisting of 90x30 cells.

The figure 2 shows the comparison of Mach number distributions on the lower wall of the GAMM channel obtained using different limiters. It is well known from numerical experiments, e.g. [12], that in the transonic regime described above, the maximum Mach number should be reached at the bottom wall of the channel in the second half of the profile with the maximum in the range $M_{\max} = 1.34 - 1.4$. Another local Mach number maximum, the so-called Zierep singularity, occurs after the shock wave. The value of the Mach number maximum, together with the resolution of the shock wave and the Zieper singularity, serve as the main criteria for assessing the quality of the numerical solution.

Table 1 shows a comparison of the maximum Mach number values obtained with different limiters in the MUSCL reconstruction and also with the result obtained using the second order WENO[7] reconstruction. The best result is achieved with the WENO scheme, followed by the Koren, MC and Superbee limiters, and by a small margin the Osher limiter with $C_\beta = 2$ and also van Leer limiter. It can be seen from the figure 3 that the best resolution of the Zierep singularity is obtained using the WENO reconstruction and also with the Superbee limiter. Slightly worse resolution is obtained with the Koren, MC and Osher ($C_\beta = 2$) limiters with minimal variation between them. The worst resolution is obtained with the the Ospre limiter.

The figures 4 and 5 show a comparison of the density residuals. The best convergence is again obtained with the WENO reconstruction and also with the van Leer limiter, with both methods achieving machine precision levels. The other limiters show stalled convergence, with the Koren and MC limiters performing best and the Ospre limiter performing worst.

Finally, it can be noted that the best results (except for the WENO reconstruction) were obtained using the MUSCL reconstruction with Koren, MC and Superbee limiters, the latter providing the best resolution but converging poorly to the stationary solution. This is followed by Osher ($C_\beta = 2$) and van Leer limiters, the latter converging very well.

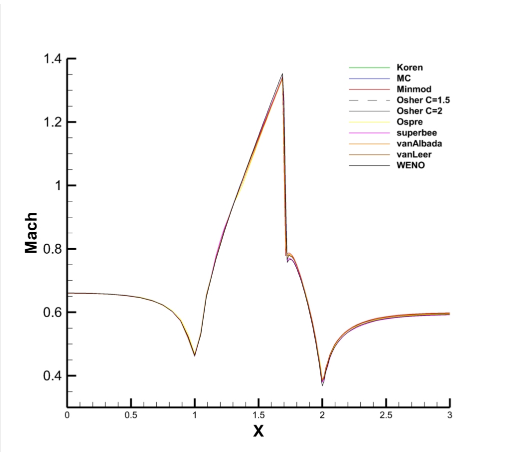

Figure 2: Mach number distribution on the lower wall of the channel.

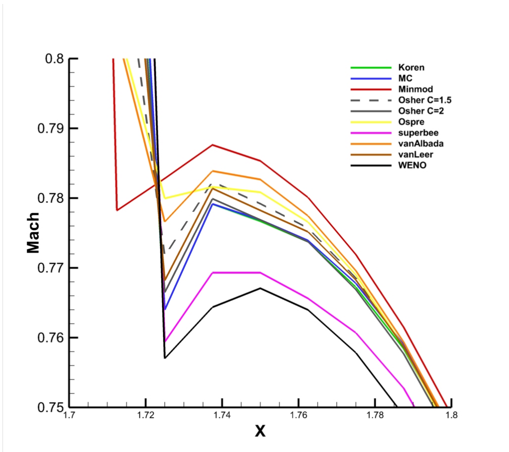

Figure 3: Detail in the vicinity of the Zierep singularity.

Mach number extremes (part 1)					
limiter	Koren	MC	Minmod	Osher, C=1.5	Osher, C=2
M_{max}	1.343	1.343	1.334	1.339	1.341

[7] Weighted Essentially Non-Oscillatory, [13].

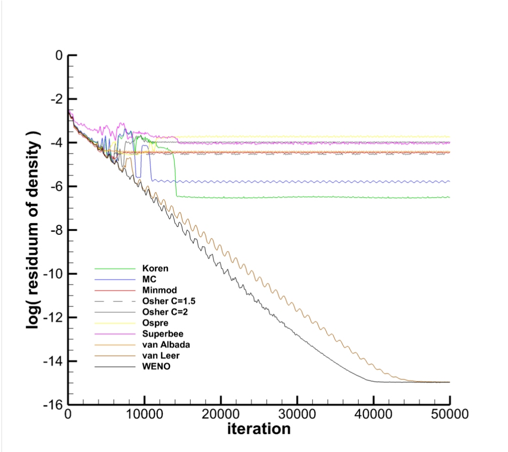

Figure 4: Density residual (dimensionless) distributions.

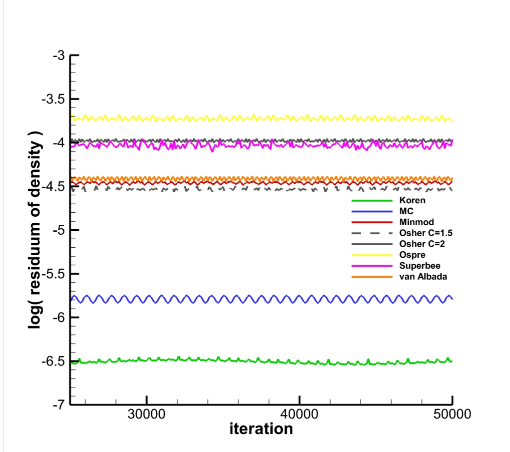

Figure 5: Detail of the density residual (dimensionless) distributions.

Mach number extremes (part2)					
limiter	Ospre	Superbee	van Albada	van Leer	WENO
M_{max}	1.335	1.343	1.335	1.341	1.353

Table 1: Mach number extremes obtained with different limiters.

5 Transonic turbulent flow past the RAE 2822 airfoil

The next solved case, the AGARD case 10 [14], where the interaction of the shock wave with the boundary layer creats a small separation region downstream of the shock, is a transonic turbulent flow characterized by the free-stream Mach number $M_\infty = 0.754$, the angle of attack $\alpha_\infty = 2.57°$ and the Reynolds number $Re = 6.2 \cdot 10^6$. The problem was solved on a domain about thirty times larger than the airfoil chord c. The domain was covered by a hyperbolically generated C-type grid with 300×70 cells, with minimum grid spacing in the y-direction $\Delta y = 5 \cdot 10^{-6}$, which corresponds to $y^+ \approx 0.5$.

The simulations using the MUSCL reconstruction with Ospre, van Albada and van Leer limiters blowed up. The figure 6 shows the comparison of the pressure coefficient distributions while the figure 7 shows the comparison of the friction coefficient distributions obtained by the MUSCL reconstruction with the rest limiters. It can be seen that the solution obtained with the Superbee limiter is very oscillatory, especially in the case of the pressure coefficient. The MC, Superbee, Osher ($C_\beta = 2$) and Koren limiters are the best at predicting the position of the shock wave, closely followed by the Osher limiter with $C_\beta = 1.5$ and also the WENO reconstruction. The Minmod limiter is relatively the worst, but the differences with the other limiters are rather small.

The figures 8 and 9 show a comparison of the density and turbulent kinetic energy residuals. The best density convergence is achieved by the WENO reconstruction and by the Osher limiter with $C_\beta = 1.5$. On the other hand, for the turbulent energy residuals, both Osher limiters are the best (the $C_\beta = 1.5$ variant performs much better) and the WENO reconstruction performs much worse, even worse than the Koren and MC limiters, almost on a par with the Minmod limiter.

In summary, the MUSCL reconstruction with the MC, Koren and Osher limiters achieves slightly better accuracy than the WENO reconstruction. The convergence of the density to the steady state is similar for all tested methods, with the WENO reconstruction and the Osher ($C_\beta = 1.5$) limiter performing best, but for the turbulent energy residuals the MC, Koren and both Osher limiters perform better than the WENO reconstruction.

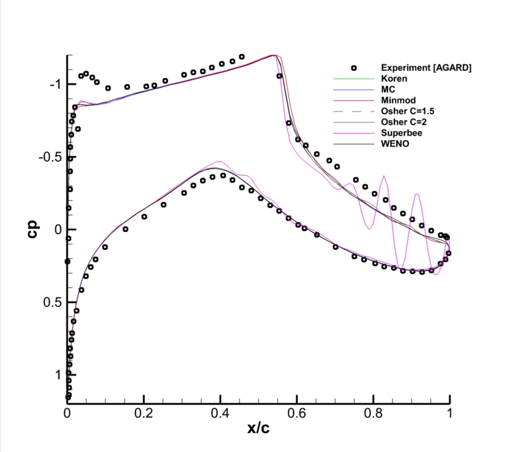

Figure 6: Pressure coefficient distributions along the airfoil.

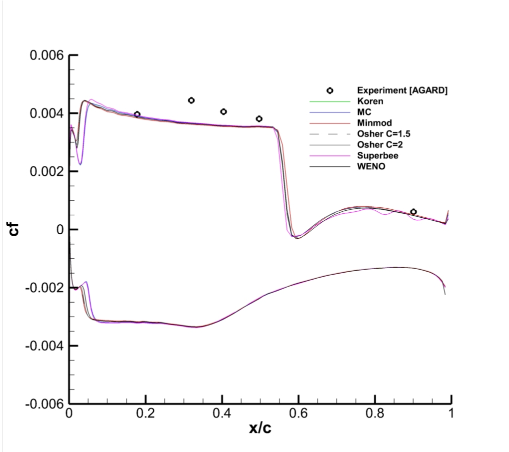

Figure 7: Friction coefficient distributions along the airfoil.

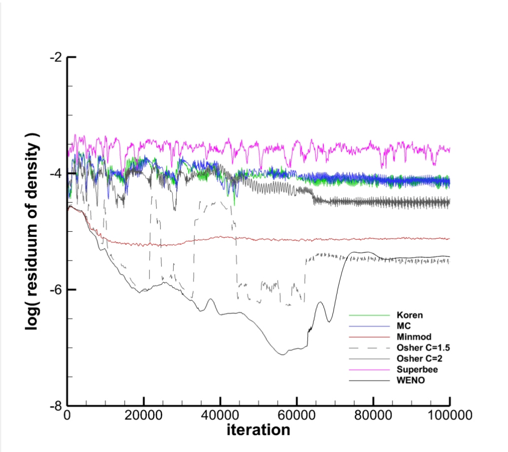

Figure 8: Density (in $kg \cdot m^{-3}$) residual distributions.

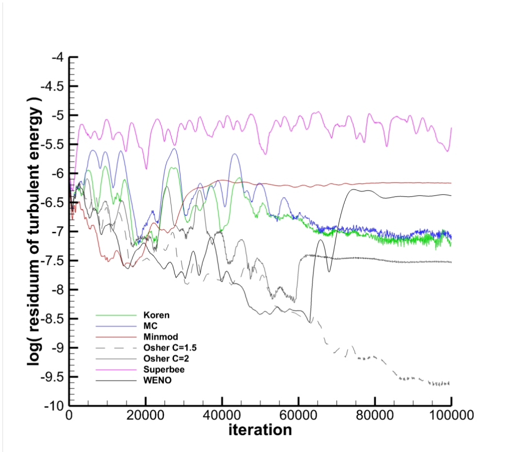

Figure 9: Turbulent energy (in $m^2 \cdot s^{-2}$) residual distributions.

6 Hypersonic viscous flow over a compressible ramp

The last solved case, the hypersonic flow over a compressible ramp is characterized by the free-stream Mach number $M_\infty = 7.7$, the Reynolds number $Re = 8.6 \cdot 10^5$ and a zero angle of attack. This setup corresponds to the same problem with the total enthalpy $H_0 = 1.7\ MJ \cdot kg^{-1}$ as in the paper [15]. The relatively low total enthalpy allows a calorically perfect gas to be used as a fluid.

The simulation was performed in the computational domain shown in figure 12 or 13. Although the geometry of the problem is simple, the solution is complex and involves the interaction of shock waves, shock wave interaction with the boundary layer, and separation, reattachment, and even transition from a laminar to a turbulent state.

The computational domain was covered by a hyperbolically generated H-type grid with 400×100 cells, with minimum grid spacing in the y-direction $\Delta y = 3.8 \cdot 10^{-6}$, which corresponds to $y^+ \approx 0.9$. In this case, a more advanced rotated-hybrid Riemann solver [7], which is based on the modified HLLC and HLL schemes, was used for the numerical solution.

The figure 10 shows distributions of the pressure coefficient along the ramp. There is a pressure increase due to boundary layer separation and to a much higher increase downstream of the reattachment location. The first increase is predicted later by all methods compared to both DNS and experiment. This is due to the much higher accuracy of the DNS method. The second increase is predicted more accurately. A qualitatively different shapes can be observed around the point x/L = 1.5. This is due to the typical sharp bypass transition[8] from the laminar to turbulent flow regime, which is notable even in the pressure distribution. Finally, the magnitude of the pressure coefficient in the turbulent part of the boundary layer is predicted in very good agreement with the DNS by all methods, although the result obtained by the MC limiter is significantly oscillatory, which is confirmed by the figure of the flow field (fig. 12). Other limiters also oscillate in the turbulent part of the boundary layer, but to a much lesser extent, see figures 13 and 10.

The figure 11 shows a comparison of the turbulent kinetic energy residuals. All limiters perform similarly, with the Osher ($C_\beta = 1.5$) limiter performing best.

In summary, the best results are obtained by the MUSCL reconstruction with the Koren and Osher ($C_\beta = 2$) limiters, which are more accurate than the results obtained with the WENO reconstruction, although both MUSCL schemes are tend to oscillate slightly in the turbulent part of the boundary layer. The method using the Osher ($C_\beta = 1.5$) limiter is almost non-oscillatory, but also less accurate than the WENO scheme.

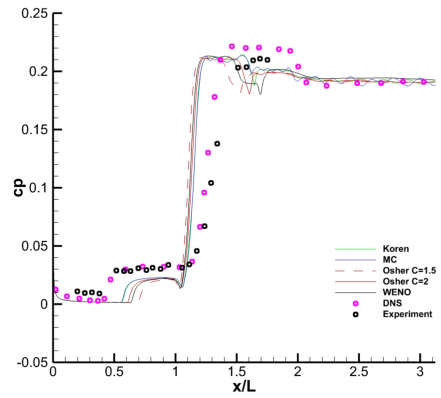

Figure 10: Pressure coefficient distributions along the ramp.

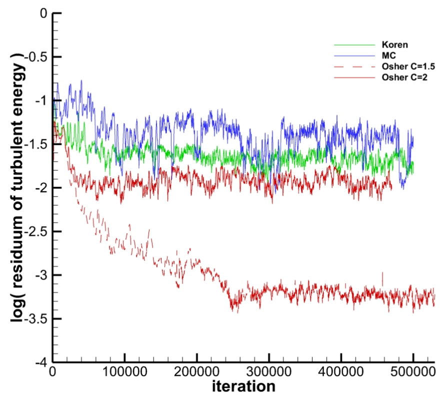

Figure 11: Turbulent energy (in $m^2 \cdot s^{-2}$) residual distributions.

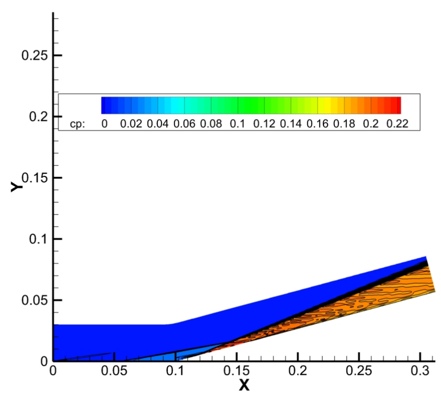

Figure 12: Pressure coefficient distribution, MC limiter.

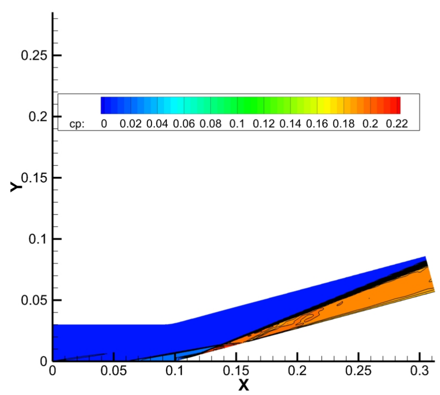

Figure 13: Pressure coefficient distribution, Osher limiter ($C_\beta = 2$)

[8]Only a simple algebraic model of the bypass transition, which is part of the modified EARSM model of turbulence, is used in this work [4].

Comparison of separation, reattachment and transition locations.						
method	Koren	MC	Osher, C=1.5	Osher, C=2	WENO	DNS
separation [x/L]	0.59	0.58	0.72	0.63	0.67	0.49
reattachment [x/L]	1.18	1.18	1.12	1.16	1.17	1.26
transition [x/L]	1.65	1.63	1.53	1.61	1.67	1.76

7 Conclusions

An analysis of the performance of limiter functions commonly used in MUSCL reconstruction was performed. From the results obtained, it seems that the best performance in high-velocity compressible viscous flow cases is obtained by the Osher or Koren limiters, where the latter tends to be more accurate, but can be oscillatory in cases with the strong shock waves, while the Osher limiter varies from the most stable (and least accurate) Minmod limiter for $C_\beta = 1$ to the most accurate form for $C_\beta = 2$ with the worst convergence, which can oscillate slightly in cases with the strong shock waves.

Acknowledgment: The author gratefully acknowledge the *Center of Advanced Aerospace Technology* (*CZ.02.1.01/0.0/0.0/16_019/0000826*) at the Czech Technical University in Prague for awarding the access to computing facilities.

References

[1] van Leer, B. and Nishikawa, H.: Towards the ultimate understanding of MUSCL: Pitfalls in achieving third-order accuracy. *Journal of Computational Physics* 446 (2021) 110640. https://doi.org/10.1016/j.jcp.2021.110640

[2] Holman, J.: Numerical Solution of Hypersonic Viscous Flow Using Rotated-Hybrid Riemann Solver. *Topical Problems of Fluid Mechanics 2024*: (2024) pp. 69-76.

[3] Holman, J. and Fürst, J.: Recalibration of TNT model for conjunction with EARSM model of turbulence. *Topical Problems of Fluid Mechanics 2012*: (2012) pp. 43-46.

[4] Holman, J. and Fürst, J.: Coupling the algebraic model of bypass transition with EARSM model of turbulence. *Advances in Computational Mathematics* 45: (2019) pp. 1977-1992. https://doi.org/10.1007/s10444-019-09680-2

[5] Holman, J. and Fürst, J.: Numerical simulation of separation induced laminar to turbulent transition over an airfoil. *Journal of Computational and Applied Mathematics* 394: (2021) 113530. https://doi.org/10.1016/j.cam.2021.113530

[6] Leveque, R. J.: Finite-Volume Methods for Hyperbolic Problems. *Cambridge University Press*, 2004.

[7] Holman, J. and Fürst, J.: Rotated-hybrid Riemann solver for all-speed flows. *Journal of Computational and Applied Mathematics* 427: (2023) 115129. https://doi.org/10.1016/j.cam.2023.115129

[8] Nishikawa, H.: A truncation error analysis of third-order MUSCL scheme for nonlinear conservation laws. *Numerical Methods in Fluids* 93 (4): (2021) pp 1031-1052. https://doi.org/10.1002/fld.4918

[9] Kuzmin, D.: On the design of general-purpose flux limiters for implicit FEM with a consistent mass matrix. I. Scalar convection, *Journal of Computational Physics* 219 (2): (2006) pp 513-531.

[10] Coirier, W.: An adaptively-refined, cartesian, cell-based scheme for the Euler and Navier-Stokes equations. *Ph.D. thesis*, University of Michigan, 1994.

[11] Isherwood, L., Grant, Z. J. and Gottlieb, S.: Strong Stability Preserving Integrating Factor Runge-Kutta Methods. *SIAM Journal on Numerical Analysis* 56, Issue 6 (2018).

[12] Feistauer, M., Felcman, J., Straškraba, I.: Mathematical and Computational Methods for Compressible Flow. *Oxford University Press*, 2003.

[13] Friedrich, O.: Weighted Essentially Non-Oscillatory Schemes for the Interpolation of Mean Values on Unstructured Grids. *Journal of Computational Physics* 144 (1998).

[14] Cook, P. H., McDonald, M. A., Firmin, M. C. P.: Aerofoil RAE 2822 - pressure distributions and boundary layer and wake measurements. *AGARD AR-138*, 1979.

[15] Holman, J.: Numerical Solution of Transition to Turbulence over Compressible Ramp at Hypersonic Velocity. *Mathematics* 2023, 11, 3684. https://doi.org/10.3390/math11173684